A Simple Multiresolution Technique for Diffraction Image Recovery

by D. Russell Luke, PIMS Postdoctoral Fellow, Simon Fraser University

We describe a Fourier-based multiresolution technique to speed up algorithms for recovering diffraction images from noisy and aberrated data. We use this method to achieve a 17-fold speed up of an adaptive optics algorithm developed by the author for an early prototype of the James Webb Space Telescope, due to replace the Hubble Space Telescope in 2011. The technique, simple and frequently rediscovered, is based on windowed Fourier transforms. While a natural strategy for our purposes, the method is not specific to our setting and can be employed in any application that uses a combination of far field scattering data and spatially dependent physical constraints.

1 Introduction

While a debate is heating up over the fate of the ageing Hubble Space Telescope [1], progress continues on Hubble's replacement, the James Webb Space Telescope (JWST) [2]. A central design feature of the JWST is *adaptive optics* capabilities that will allow the telescope to fine-tune itself during observations. To accomplish this, the telescope will combine computational wavefront sensing techniques together with deformable mirrors to detect and correct for system aberrations. In the past, wavefront sensing was performed by an intricate labyrinth of hardware. The JWST marks the beginning of a shift toward computational techniques that are a dividend of efforts to find and correct for the manufacturing defect that plagued Hubble's early days.

The problem of wavefront sensing is just one instance of a common problem in imaging known as phase retrieval. In broad terms, one is faced with recovering, from intensity measurements alone, the geometric path of propagation of a wave that has interacted with some scattering material or medium. In mathematical terms, the phase problem amounts to finding the real and imaginary parts of a complex-valued scalar function from knowledge of its amplitude before and after being acted upon by a unitary linear operator. The problem has been around at least since the 1890's [3], and breakthroughs in the early 1950's for scattering from periodic structures [4–6] earned Hauptman and Karle the Nobel Prize in Chemistry in 1985. The phase problem is far from solved, however, in any analytical sense for general settings. Nevertheless the problem has been solved *numerically* for over three decades [7, 8] even though there is still no proof that the most popular techniques should work at all, let alone so well [9, 10]. It is to this happy circumstance that Hubble owes some of its success, since without phase retrieval algorithms it might have been impossible to pinpoint fabled flaw in Hubble's original primary mirror [9].

We show the flavor of this problem by way of a discussion of a Fourier-based multiresolution technique for decreasing the cpu-time for computational wavefront sensing from noisy and aberrated data. We use this method to achieve a 17-fold speed up of an adaptive optics algorithm developed by the author for an early prototype of the JWST. Though often forgotten, the technique is a well understood tool based on windowed Fourier transforms. A natural strategy for our purposes, the method is not specific to our setting and can be employed in any application that uses a combination of far field scattering data and spatially dependent physical constraints. For a more detailed review of diffraction imaging we refer the reader to [9] and references therein. The extension of these ideas to obstacle scattering as described in [11] is a topic of current research.

2 Phase retrieval

The *forward imaging* model is formulated on the space of square integrable functions mapping $\mathbb{R}^2$ to $\mathbb{C}$. The model input $u : \mathbb{R}^2 \to \mathbb{C}$ is an electromagnetic field generated by the object we are trying to observe. We call the domain of u the *physical domain*. The device through which the wave travels is characterised by a modified Fourier transform $\mathcal{F}_m$ of the form

$$(\mathcal{F}_m u)(\xi) \equiv \int_{\mathbb{R}^2} u(x) e^{i\left(2\pi x\cdot\xi + \tilde{\theta}_m(x)\right)}\, dx \tag{1}$$

The function $\tilde{\theta}_m : \mathbb{R}^2 \to \mathbb{R}$ for $m = 1, 2, \ldots, M$ is a phase *aberration* that models a known device tuning such as defocus. The model output, or data, corresponding to the mth tuning of the device are amplitude measurements, $\psi_m : \mathbb{R}^2 \to \mathbb{R}_+$, where $\mathbb{R}_+$ denotes the non-negative orthant. Due to the relations between the image ψ_m and the Fourier transform, we refer to the domain of the image as the *frequency domain*. The data ψ_m are often referred to as the frequency domain *magnitude constraints* of the imaging model.

Just before the wave passes through our instrument, it is assumed that $|u| = A$ where $A : \mathbb{R}^2 \to \mathbb{R}_+$ and the modulus $|\cdot|$ is the *pointwise Euclidean* magnitude. This is known as the *entrance pupil constraint*. For convenience, we denote

$$\mathcal{F}_0 \equiv \mathcal{I} \quad \text{and} \quad \psi_0 \equiv A \tag{2}$$

where $\mathcal{I}$ is the identity operator. The imaging model is then given by

$$|\mathcal{F}_m u| = \psi_m, \quad m = 0, 1, \ldots, M. \tag{3}$$

The *inverse problem* with which we are concerned is to solve (3) for u given $\mathcal{F}_m$ and ψ_m. Whatever method one has for solving this problem, the next section details a strategy for obtaining low resolution estimates first, and using these as a bootstrap to higher resolution solutions.

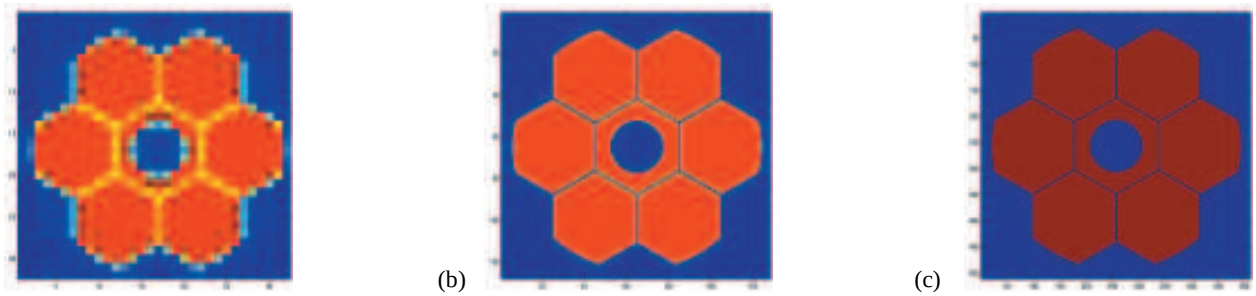

Figure 1: Multi-Resolution entrance pupil constraints, at (a) 32 x 32 resolution corresponding to the 32 x 32 image data shown in Fig.(2), (b) 128 x 128 resolution corresponding to the 128 x 128 image data, and (c) 512 x 512 resolution.

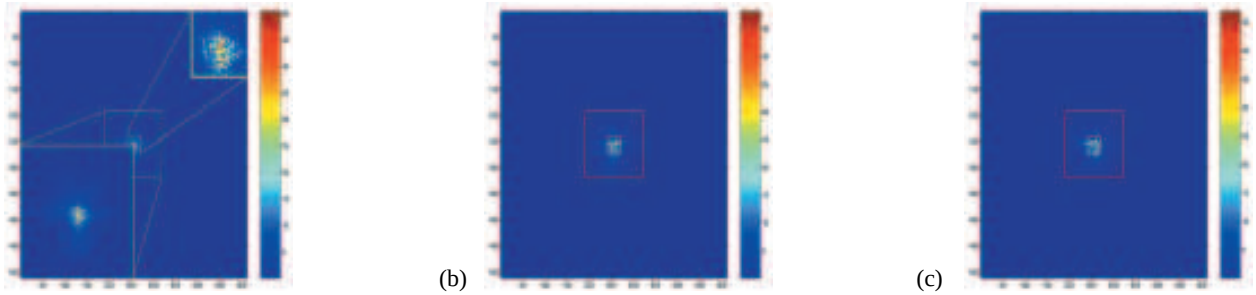

Figure 2: Multi-resolution image data. Three levels of multiresolution windowing operations are depicted for each diversity image. Frame (a) shows close-ups of each of the three resolution levels. The centre 32 x 32 pixels of each diversity image, together with the corresponding low-resolution entrance pupil constraint Fig. (1.a) are used to generate the approximate solution shown in Fig. (3.a). This solution is used to initialize the same problem with the centre 128 x 128 pixels and the corresponding mid-resolution entrance pupil constraint (Fig. (1.b)) as data. The solution to this problem, shown in Fig. (3.b), is used to initialize the full resolution problem. The progress of the error metric versus iteration of the multiresolution implementation is shown in Fig. (5).

3 A multiresolution strategy

We motivate this method with a discussion of filtering, and show the corresponding interpretation as a multiresolution analysis.

Noise often dominates high frequency components of an image $\psi_m(\xi)$. A common technique for reducing or *filtering* noise is to truncate the images and set all high frequency components to zero, that is, to set $\psi_m(\xi) = 0$ for $\|\xi\|_\infty > a$, for some cutoff $a > 0$. For the imaging model given by Eq. (3), the image ψ_m is the magnitude of the modified Fourier transform of the field u. Thus the filtering operation just described amounts to multiplying the Fourier transform of u by a *window* or characteristic function of the box of length $2a$ in the frequency domain. Suppose the domain is sampled on square pixels of length Δx. Let $\mathcal{X}_n$ denote the indicator function for the $n \times n$ box of pixels centred at zero, where, for convenience, n is a multiple of 2. For a sampled image ψ_m centred at zero we have the following system of equations for the windowed image

$$\mathcal{X}_n \odot |\mathcal{F}_m u| = \mathcal{X}_n \odot \psi_m, \quad m = 1, \ldots, M. \tag{4}$$

where $\odot$ represents the discrete Hadamard matrix product and $\mathcal{F}_m$ $(m = 1, \ldots, M)$ are the discrete counterparts of the continuous operators defined in Eq. (1). Note that the window is *not* applied to the physical domain equation ($m = 0$) given by Eq. (2) and Eq. (3). This has to do with the relation between the truncation of high frequency Fourier modes and blurring in the physical domain. This discussed in more detail below.

The multiresolution approach relies on our ability to write the left hand side of Eq. (4) as a localized average of nearby pixels of $ue^{i\tilde{\theta}_m}$. Since the Hadamard product commutes with the pointwise modulus function we can write the windowed function on the right-hand side of Eq. (4) as $\mathcal{X}_n \odot |\mathcal{F}_m u| = |\mathcal{X}_n \odot \mathcal{F}_m u|$. For $m \geq 1$, by the Discrete Convolution Theorem, we have

$$|\mathcal{X}_n \odot \mathcal{F}_m u| = \left| \left(\mathcal{X}_n^\vee * \left(ue^{i\tilde{\theta}_m} \right) \right)^\wedge \right| \quad m = 1, \ldots, M.$$

Here $\wedge$ and $\vee$ indicate the discrete Fourier transform and its inverse respectively.

In 2-dimensions, the Fourier transform of the window function is a product of sinc functions of each of the components separately.

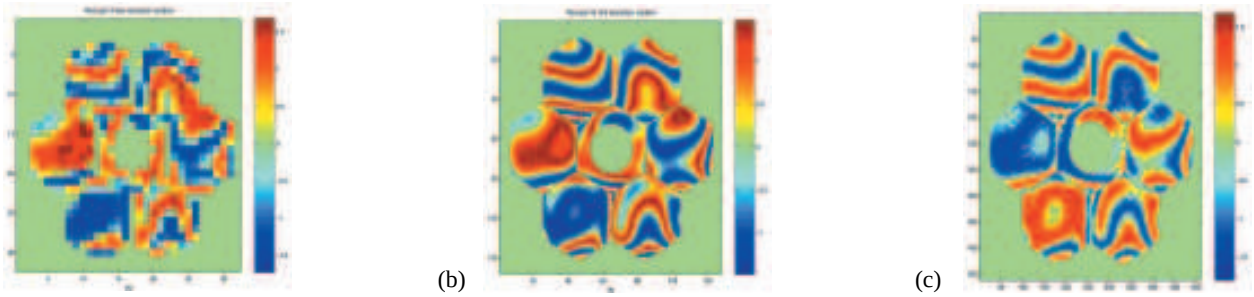

Figure 3: Aberrated wavefront for the segmented pupil recovered from 3 diversity point source images on successively finer grids. The real part of the low resolution wavefront (a) is generated from a truncation of the image data to the centre 32 x 32 pixels. This solution is used as a first guess for the next resolution, 128 x 128. The 128 x 128 pixel resolution solution (b) is used as a first guess for the full resolution problem whose solution is shown in (c).

For $x \in \mathbb{R}^2$

$$\text{sinc}\left((n\Delta x)\, x\right) \equiv \frac{sin\left((\pi n\Delta x)x_1\right)}{(\pi n\Delta x)x_1} \times \frac{sin((\pi n\Delta x)x_2)}{(\pi n\Delta x)x_2} = \frac{1}{n\Delta x}\mathcal{X}_n^{\vee}.$$

Convolution against a sinc function, $\mathcal{X}_n^{\vee}$, can be approximated by a localized discrete linear operator, $\mathcal{A}_n$, that averages blocks of adjacent pixels. For the moment we leave the definition of $\mathcal{A}_n$ ambiguous – many different averaging operators are possible. For $m \geq 1$ the convolution on the right hand side of Eq. (4) can therefore be approximated by $\mathcal{X}_n^{\vee} * \left(ue^{i\tilde{\theta}_m}\right) \approx \mathcal{A}_n\left(ue^{i\tilde{\theta}_m}\right)$. This yields the following approximation of Eq. (4)

$$\left|\left(\mathcal{A}_n\left(ue^{i\tilde{\theta}_m}\right)\right)^{\wedge}\right| \approx \mathcal{X}_n \odot \psi_m, \quad m = 1, \ldots, M. \tag{5}$$

The filtering operation applied to the images ψ_m $(m = 1, \ldots, M)$ cannot be directly applied to the physical domain constraint represented by the "image" ψ_0. The analog in the physical domain is an averaging operation. To see this consider the (discrete) Fourier dual of the physical constraint $|u|^{\wedge} = \psi_0^{\wedge}$. Now, apply the window $\mathcal{X}_n$ to get $\mathcal{X}_n \odot |u|^{\wedge} = \mathcal{X}_n \odot \psi_0^{\wedge}$. Again, by the Discrete Convolution Theorem the Fourier dual of the windowing operation, *i.e.* the filtering operation in the physical domain, is given by $\mathcal{X}_n^{\vee} * |u| = \mathcal{X}_n^{\vee} * \psi_0$. We approximate the right hand side of this equation by $\mathcal{X}_n^{\vee} * |u| \approx \mathcal{A}_n |u|$. This yields the approximate physical domain relation corresponding to the application of a window in the Fourier domain,

$$\mathcal{A}_n |u| \approx \mathcal{X}_n^{\vee} * \psi_0. \tag{6}$$

Equations (5) and (6) constitute a low resolution imaging system. The averaging operator $\mathcal{A}_n$ blurs information in adjacent pixels of the wavefront estimate u, smoothing out edges as well as noise. It is not necessary, therefore, to maintain a high pixelization for the wavefront estimate u since fine detail is lost by averaging. In Eq. (5) only the centre n pixels of the image are kept in the calculation. Our implementations rely on the Fast Fourier Transform Algorithm (FFT) to calculate the discrete Fourier transforms. These require square arrays with dimensions that are powers of 2. Our computations take advantage of the lower resolution image by using a pixelization of u that is consistent with the size of the window $\mathcal{X}_n$. This dramatically reduces the dimensionality of the optimization problem and thus computation time. It cannot be expected that the solution to the low resolution problem will be as good as the high resolution, however, we use the low resolution solutions as a bootstrap to higher resolution estimates. Ideally, all of the hard work is done at low resolution and relatively few iterations are necessary to achieve a solution at the highest resolution. This is indeed what we achieve (see Fig. (5)).

4 Numerical Results

The aperture design for one of several prototype telescopes studied at NASA's Goddard Space Flight Center for the JWST is shown in Fig. (1).

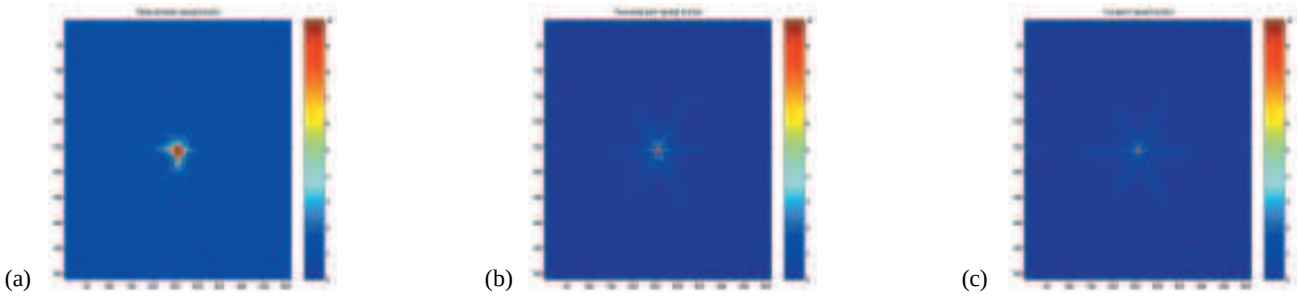

Figure 4: Noisy point-spread function (a) for a segmented pupil on a 512 x 512 grid. The recovered point-spread function (b) was first filtered with a Fourier window filter before processing by the wavefront reconstruction algorithm. Frame (c) shows the true, unaberrated point-spread function.

In Fig. (2.a) a series of windowing operations is depicted for the three 512×512 diversity images. First, the centre 32×32 pixels of each diversity image are kept, and the remaining pixels are set to zero, that is for $m = 1, 2, 3$, we set

$$\widetilde{\psi_m} = \mathcal{X}_{32} \odot \psi_m.$$

The corresponding physical domain operation is to smooth the entrance pupil constraint by convolution with the sinc function. This is achieved by setting

$$\widetilde{\psi_0} = \left(\mathcal{X}_{32} \odot \psi_0^{\wedge}\right)^{\vee}.$$

The resulting entrance pupil constraint is depicted in Fig. (1.a). For $m = 1, 2, 3$, the dimension reduction of the images $\widetilde{\psi_m}$ is straight forward. One simply ignores the zero pixels outside of the window. In the physical domain the reduction of dimension is achieved by assigning single values to blocks of 16×16 adjacent pixels. In our implementations the value that is assigned is the average of the 16^2 pixels. The corresponding wavefront reconstruction problem is $1/16$ the original problem size. The solution corresponding to this resolution is depicted in Fig. (3).

The next step is to use the solution depicted in Fig. (3) as an initial guess for the next resolution, which in this example is 128×128 pixels. To do this, one simply divides the pixels of the low resolution solution into 16 sub-pixels. the image and physical domain data are treated the same as with the 32×32 case. The solution to the 128×128 problem is then used as the initial guess for the full resolution problem. The conjugate of the phase recovered in Fig. (3.c) is generated via deformable mirrors in the telescope in order to achieve the nearly diffraction limited *point spread function* shown in Fig. (4.b).

In Fig. (5) the squared set distance error versus iteration for a multiresolution implementation of a limited memory BFGS algorithm with trust regions to solve an extended least squares problem developed by the author [9, Sec. 5.3 and Alg.6.2] is shown. Notice that the flat region of the error metric indicating algorithm stagnation (typical for this problem) is encountered at low resolution. The higher resolution runs are started in a neighbourhood of the solution and very few iterations are required for convergence. All of the hard work is accomplished cheaply at low resolutions. Starting from an initial phase guess of zero, the multiresolution implementations reduced cpu-time by a factor of 17 over the full resolution run.

References

[1] D. Overbye As clock ticks for Hubble, some plead for a reprieve, *The New York Times*, July, 27, 2003.

[2] James Webb Space Telescope homepage `http://www.jwst.nasa.gov/`.

[3] Lord Rayleigh (J. W. Strutt), On the interference bands of approximately homogeneous light; in a letter to Prof. A. Michelson, *Phil. Mag.*, **34**:407–411 (1892).

[4] D. Sayre, Some implications of a theorem due to Shannon, *Acta Crystallogr.* ACCRA9 5, 843:60-65 (1952).

[5] H. Hauptman, Direct methods and anomolous dispersion – Nobel lecture, 9 December 1985, *Chemica Scripta* **26**(2): 277-286 (1986).

[6] J. Karle, Recovering Phase information from intensity data – Nobel lecture, 9 December 1985 *Cemica Scripta* **26**(2): 261-276 (1986).

[7] J. Fienup. Phase retrieval algorithms: a comparison. *Appl.Opt.*, 21(15):2758–2769, 1982.

[8] R. Gerchberg and W. Saxton. A practical algorithm for the determination of phase from image and diffraction plane pictures. *Optik*, 35:237–246, 1972.

[9] D. R. Luke, J. V. Burke, and R. Lyon. Optical wavefront reconstruction: theory and numerical methods. *SIAM Review*, 44:169–224, 2002.

[10] H. H. Bauschke, P. L. Combettes, and D. R. Luke. Phase retrieval, error reduction algorithm, and Fienup variants: A view from convex optimization. *J. Opt. Soc. Amer. A*, 19(7):1334-1345 (2002).

[11] D. R. Luke, Multifrequency inverse obstacle scattering: the point source method and generalized filtered backprojection, *Mathematics and Computers in Simulation* (to appear).
Download: `www.pims.math.ca/publications/preprints/`.

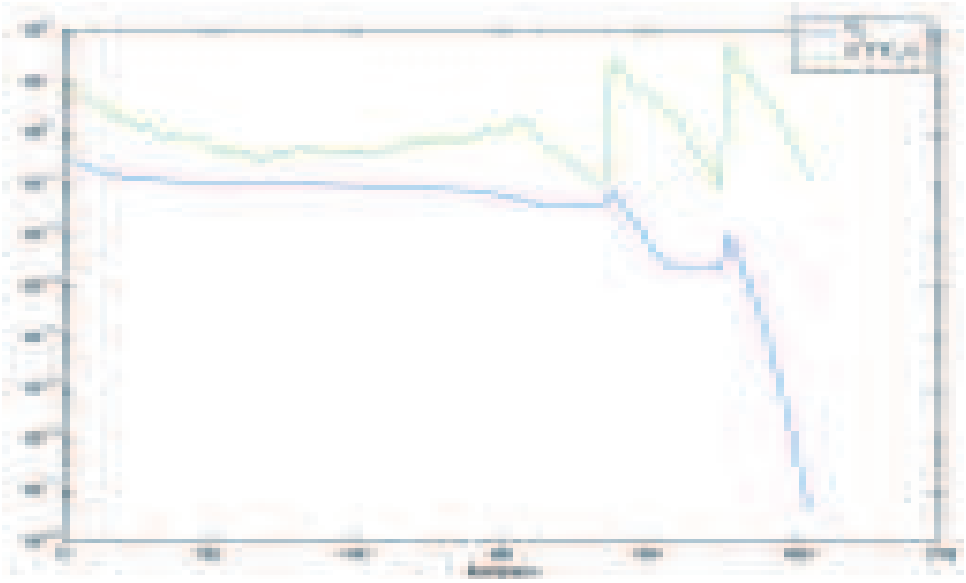

Figure 5: Error metric and corresponding norm of the gradient versus iteration for a multiresolution implementation of the limited memory BFGS algorithm with trust regions applied to an extended least squares problem discussed in [9, Sec. 5.3 and Alg. 6.2]. The flat region of the iterations is handled at low resolutions. Only when the estimate is in the neighbourhood of a solution does the algorithm switch to higher resolution calculations.